



Article

Construction of Urban Thermal Environment Network Based on Land Surface Temperature Downscaling and Local Climate Zones

Xueling Zhang ¹, Alimujiang Kasimu ^{1,2,3,*} , Hongwu Liang ¹ , Bohao Wei ¹ , Yimuranzi Aizizi ¹ ,
Yongyu Zhao ¹ and Rukeya Reheman ¹

¹ School of Geography and Tourism, Xinjiang Normal University, Urumqi 830054, China

² Research Centre for Urban Development of Silk Road Economic Belt, Xinjiang Normal University, Urumqi 830054, China

³ Xinjiang Key Laboratory of Lake Environment and Resources in Arid Zone, Urumqi 830054, China

* Correspondence: alimkasim@xjnu.edu.cn; Tel.: +86-150-9907-9312

Abstract: It has become undeniable that global land surface temperature (LST) has continued to rise in recent years. The threat of extreme heat to humans has become self-evident, especially in arid regions. Many studies have clarified the temperature rise/fall mechanism of LST from the perspective of influencing factors. However, there are few studies on mitigating LST from the standpoint of regional networks. This paper first combines Landsat 8 with Sentinel-2 imagery for LST downscaling based on the Google Earth engine as a way to match local climate zone (LCZ) with 17 classification types. Then, the thermal environment resistance surface is constructed according to LCZ, and the essential cold sources are identified using morphological spatial pattern analysis (MSPA) and circuit theory to form the thermal environment green corridor and obtain the pinch point and barrier point areas. The results show that (1) The downscaling of LST based on random forest (RF) for the Urumqi–Changji–Wujiaqu metropolitan area has an R^2 of 0.860 and an RMSE of 3.23, with high downscaling accuracy. (2) High temperature (HT), medium temperature (MT), and low temperature (LT) have the largest proportions in the study area; HT dominates in Urumqi, LT in Changji, and MT in Wujiaqu. (3) The natural types (LCZ-D, LCZ-C, and LCZ-F) in the LCZ classification occupy a large area, and the building types are mainly concentrated in Urumqi; LCZ-D, LCZ-G, and LCZ-A contribute the most to the cooling of LST, and LCZ-F, LCZ-C, and LCZ-10 contribute the most to the warming of LST. (4) After identifying critical cold source patches according to MSPA to arrive at 253 green corridors, subsensitive corridors and sensitive corridors need to take certain measures to prevent corridor blockage; pinch point areas, as well as barrier point areas, need to be protected and repaired according to their respective characteristics. In summary, corresponding cooling measures to specific areas can improve the connectivity between cooling sources and slow down the temperature increase of the whole area. This study and experimental approach can provide new insights for urban planners and climate researchers.

Keywords: land surface temperature; downscaling; local climate zone; thermal environment network



Citation: Zhang, X.; Kasimu, A.; Liang, H.; Wei, B.; Aizizi, Y.; Zhao, Y.; Reheman, R. Construction of Urban Thermal Environment Network Based on Land Surface Temperature Downscaling and Local Climate Zones. *Remote Sens.* **2023**, *15*, 1129. <https://doi.org/10.3390/rs15041129>

Academic Editors: Guangdong Li, Sanwei He and Zhiqi Yang

Received: 22 December 2022

Revised: 15 February 2023

Accepted: 16 February 2023

Published: 18 February 2023



Copyright: © 2023 by the authors. Licensee MDPI, Basel, Switzerland. This article is an open access article distributed under the terms and conditions of the Creative Commons Attribution (CC BY) license (<https://creativecommons.org/licenses/by/4.0/>).

1. Introduction

Land surface temperature (LST) is a “schematic” depicting the flow of matter and energy between the land surface, the atmospheric insulation layer, and solar radiation [1,2]. It is well known that the temperatures in the downtown areas of most major cities are greater than those in the surrounding suburbs [3]. This phenomenon is collectively referred to as the urban heat island (UHI) effect [4,5]. In addition, some research has shown that the size of the UHI varies seasonally due to changes in sun intensity [6], ground cover [7], and weather [8]. Because of this variation, UHI is usually the greatest in summer [9,10]. The detrimental effects of the UHI effect are, without a doubt, enormous in summer

too. Residents of the core region of UHI are subjected to high-temperature stress for an extended period of time, which will increase the prevalence of heat stroke and the likelihood of mortality [11]. In light of this, research on the distribution of LST at the urban scale is crucial for fostering urban ecological security, enhancing human well-being, and controlling urban microclimates.

The thermal infrared band carried by satellite sensors provides a technical means for monitoring the thermal environment of the Earth's surface [12,13]. Among them, MODIS and Landsat are the most significant methods to invert the surface temperature, and their spatial resolutions of 1000 m and 30 m, respectively, satisfy the observational needs of large-scale and mesoscale LST variations [14,15]. It is insufficient, however, to support the spatial heterogeneity of LST and urban land cover types (high, medium, and low-rise structures; impervious surfaces such as airports and asphalt) inside the city [16,17]. In order to address this need, LST downscaling research has garnered some attention in recent years [18,19]. LST downscaling utilizes the low spatial resolution pixel value as an explanatory variable for the fusing of high spatial resolution to acquire more specific spatial information about ground objects [20]. Statistical regression downscaling approaches, such as the DisTrad algorithm [21,22], TsHARP algorithm [23], and HUTS algorithm [24], implement LST downscaling by utilizing the connection between LST and regression statistical models. Furthermore, emerging machine learning algorithms are more robust for building models with intricate relationships [25]. Compared to machine learning approaches such as artificial neural networks (ANN) and support vector machines (SVM), random forests (RF) are better suited for urban-scale downscaling studies due to their minimal operation and huge capacity [26,27].

Additionally, for a long time, the UHI definition of "urban" and "rural" at the urban scale has been measured by temperature differential [28]. However, this separation is no longer always clear-cut, as urban versus rural is not simply a matter of population accumulation [29]. In addition, there is a special presence in the thermal environment, namely the oasis "cold island", which means that the oasis area is a "cold source" compared to the surrounding environment (bare ground such as desert and hay-like vegetation) [30]. Different regions of the same country have different urban spatial morphological structures, and the traditional UHI division is clearly flawed; therefore, there is a need to understand the urban land use structure in a standardized way [31]. Stewart and Oke's [32] local climate zone (LCZ) concept transforms the division of UHI from a binary structure to a three-dimensional structure that can objectively reflect the spatial morphology and covering properties of urban and rural areas. The LCZ framework has developed a series of quantitative indicators based on differences in land use status, the nature of the underlying surface, the structure of above-ground buildings, and the degree of human aggregation and has classified urban underlayment into ten types of buildings and seven types of natural cover, for a total of 17 categories [33]. The advent of the LCZ framework provides the theoretical groundwork for regional and even global comparisons of UHI intensity [34]. Concerning, is the fact that as cities and towns expand, the oasis "cool source" in dry regions is diminishing, and city dwellers in arid zones face tremendous heat stress issues [35]. Consequently, the research of UHI based on LCZ theory is extraordinarily significant to the issue of thermal environment management in arid regions.

Then, after sorting out the boundaries of the UHI, how to identify the cold heat island patches network structure of the urban thermal environment, so as to mitigate the disadvantages brought by UHI and take specific measures, becomes a key objective to cope with extreme climate change and improve the habitat for humanity. A part of this objective, scholars use the urban blue-green space (water, wetland, and green space) system to characterize a new indicator of the urban cold island effect [36]. However, there are regional variations in the blue-green space cold island effect due to the various landscape and space structures, such as terrain, underlying surface, and land cover, between the urban core, urban fringe, and suburban areas [37]. Scholars have also combined methods such as spatial morphology and landscape ecology to identify different spatial

scale corridors and the spatial networks formed by their interactions for urban thermal environment research [38–40]. Morphological Spatial Pattern Analysis (MSPA) can quantify the internal connectivity of plaques and accurately classify the types of plaques that have the characteristics of emphasizing ecological processes and ecological networks [41,42]. In the meantime, circuit theory can successfully compensate for MSPA's lack of functional connection and is also utilized to determine key corridors [43]. In conclusion, the research about UHI cannot be limited to the spatial and temporal variation of LST, the cooling measures of the green landscape, and the driving of LST by the influencing factors, etc.; it is also vital to research the formation mechanism within the complex system of the urban thermal environment and the value function of the spatial network.

In summary, this paper uses the Urumqi–Changji–Wujiaqu metropolitan area in Xinjiang, China as the study area, investigates the distribution of LST from the perspective of urban spatial morphological structure based on LST downscaling and LCZ theory, and constructs an urban thermal environment network utilizing MSPA and circuit theory. The purpose of this study is to judge the heat storage capacity of the urban spatial form, identifying the key nodes of the thermal environment network, and effectively mitigating the UHI effect based on the thermal environment network.

2. Materials and Methods

2.1. Study Area

Urumqi–Changji–Wujiaqu City is the most significant metropolitan area in northwestern China, located at the foot of the Tianshan Mountain Range and southeast of Junggar Basin, with an average altitude of about 800 m (Figure 1). The research region is bordered by three mountains: Boda Mountain to the east, Karaza Mountain to the west, and Ilenhaberga Mountain to the south [44]. The interior of the study area is primarily a plain with open terrain, gentle undulations, and an overall “trumpet-shaped” distribution. From the Köppen climate classification, the arid climate (B) is a typical climate in northwestern China. The study area is far from the ocean, with high temperatures and dryness in summer and severe cold and little rain in winter, and the climate types are mainly cold desert climate (BWk) and cold steppe climate (BSk) [45]. Despite being located in an inland arid zone, the study area is rich in above-ground glacial resources and groundwater resources, and as a result, it has nurtured oasis ecosystems that are habitable for humans. The Urumqi–Changji–Wujiaqu metropolitan area is a significant node on the economic belt of the Second Asia–Europe Continental Bridge and a vital hub for economic, cultural, and ecological interchange in western China. Due to its proximity to Central Asian countries, the metropolitan area has a strong radiation effect and comprehensive influence on the entire Xinjiang and Central Asian regions.

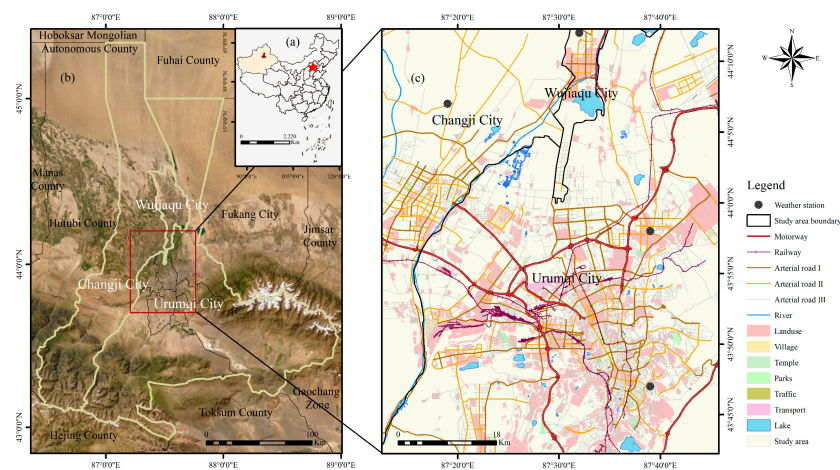


Figure 1. Location of the study area: (a) China; (b) Urumqi–Changji–Wujiaqu metropolitan area; (c) Urumqi–Changji–Wujiaqu metropolitan area partial.

2.2. Data and Source

In this paper, based on the remote sensing data cloud platform (<https://earthengine.google.com/>) (accessed on 10 September 2022), Landsat-8 (L8), and Sentinel-2 (S2), remote sensing images on 7 August 2021 were selected with a spatial resolution of 30 m and 10 m, respectively. Both L8 and S2 cloud amounts are less than 5. After image preprocessing, LST downscaling is performed, and the accuracy is compared with the weather station data (<https://www.resdc.cn/>) (accessed on 2 October 2022). The remaining data, including roads, water systems, and other vector data, are sourced from OSM (<https://www.openstreetmap.org/>) (accessed on 10 October 2022), whilst building data are crawled from the Baidu Map (<https://map.baidu.com/>) (accessed on 11 October 2022). The specific research steps are shown in the figure below (Figure 2).

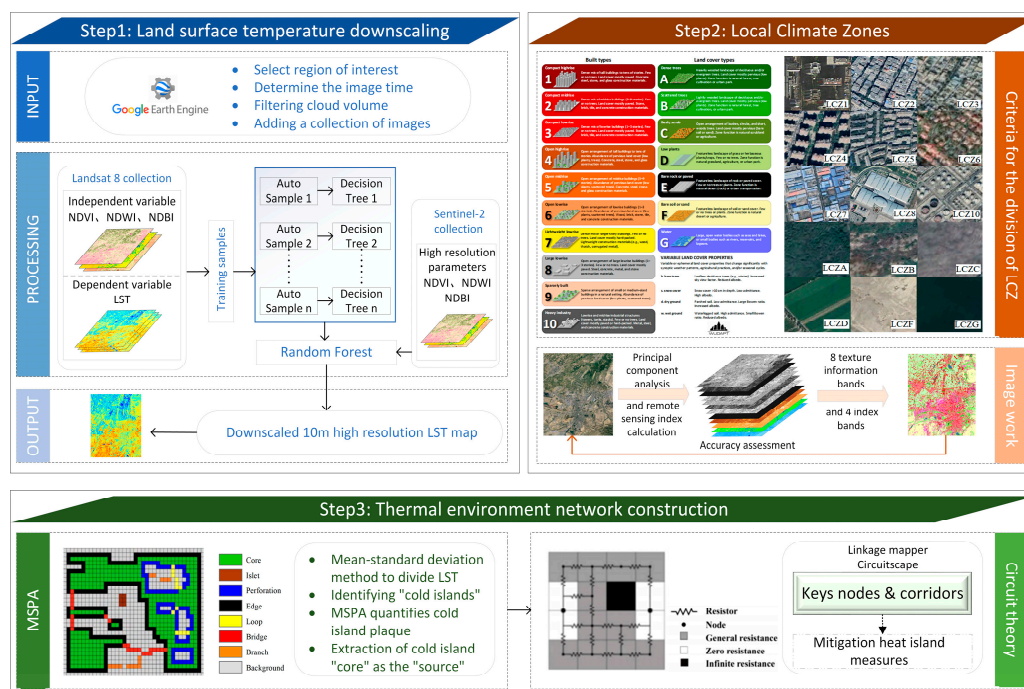


Figure 2. Research Framework Diagram.

2.3. LST Downscaling

The random forest (RF) method is a machine learning algorithm based on classification decision trees [46]. Classification decision trees are constructed for each individual decision tree based on the number of training samples selected, and the final regression results are determined by averaging the voting results of all decision trees [47,48]. The essence of constructing the RF model is a regression problem. In the downscaling process, there is a nonlinear relationship between the LST and each explanatory variable [49]. In contrast, the RF downscaling model is not sensitive to multicollinearity and can deal with the problem of overfitting very well. Consequently, the choice of explanatory variable is of utmost importance. In this study, the RF model is constructed based on the Google Earth engine. The training samples are relatively low-resolution L8 remote sensing images (30 m); LST is the dependent variable, and NDVI, NDBI, and NDWI are explanatory variables (Table 1 and Figure 3). The high spatial resolution S2 surface parameters (10 m) are input into the constructed RF model to obtain high spatial resolution (10 m) LST prediction results [29]. Then, the LST downscaling results (10 m resolution) are obtained after inputting the fitted residuals resampled to high spatial resolution.

Table 1. Downscaling process applied surface parameters.

Variables	Acronym	Formulation
Normalized difference Vegetation index	NDVI	$\frac{NIR-Red}{NIR+Red}$
Normalized difference Built-up index	NDBI	$\frac{SWIR-NIR}{SWIR+NIR}$
Normalized difference Water index	NDWI	$\frac{Green-NIR}{Green+NIR}$

NIR is the near-infrared band; *Red* is the red band; *SWIR* is the short-wave infrared band; *Green* is the green band.

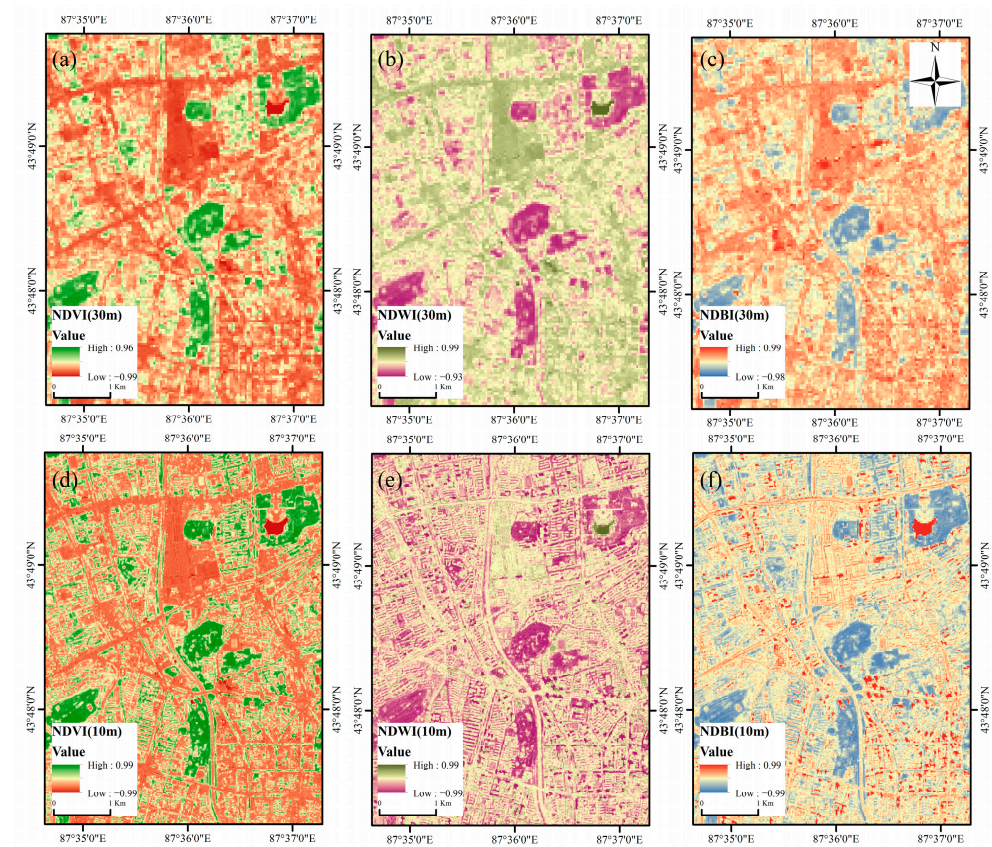


Figure 3. Local comparison of surface parameters: (a) NDVI, (b) NDWI, and (c) NDBI are L8 30 m resolution parameters; (d) NDVI, (e) NDWI, and (f) NDBI are S2 10 m resolution parameters.

For Landsat8 TIRS, B11 band inversion parameters are not ideal with uncertainty, so B10 band inversion LST [50] is generally used:

$$L_{\lambda} = [\varepsilon \cdot B(T_s) + (1 - \varepsilon)L_{\downarrow}] \cdot \tau + L_{\uparrow} \quad (1)$$

where ε is the surface-specific emissivity; $B(T_s)$ is the thermal radiation intensity of a blackbody at the same temperature; T_s is the true LST; and the atmospheric transmittance τ , atmospheric downward radiance L_{\downarrow} , and atmospheric upward radiance L_{\uparrow} in the thermal infrared band can be obtained through NASA's official website.

After converting the Kelvin degree of LST into Celsius degree, the high spatial resolution LST is obtained based on the idea that the functional relationship between LST and its surface parameters remains constant at different scales [27]:

$$T_{HR} = f(S_{HR}) + \Delta T_{LR} \quad (2)$$

$$\Delta T_{LR} = T_{LR} - f(S_{LR}) \quad (3)$$

where: S_{HR} and S_{LR} are the surface parameters of S8 and L8, respectively; f is the mapping relationship between surface temperature T_{HR} (T_{LR}) and surface parameter S_{HR} (S_{LR}) at different scale spatial resolutions; and ΔT_{LR} is the residual. This paper uses the mean-standard deviation method to classify the LST downscaling results (Table 2).

Table 2. LST classification level table.

LST Level	Acronym	Classification Range
Extremely low temperature	ELT	$T < \mu - 1.5 \text{ std}$
Low temperature	LT	$\mu - 1.5 \text{ std} \leq T < \mu - 0.5 \text{ std}$
Medium temperature	MT	$\mu - 0.5 \text{ std} \leq T < \mu + 0.5 \text{ std}$
High temperature	HT	$\mu + 0.5 \text{ std} \leq T < \mu + 1.5 \text{ std}$
Extremely high temperature	EHT	$T > \mu + 1.5 \text{ std}$

T is the LST value, μ is the mean, and std is the standard deviation.

Finally, The LST obtained from the L8 inversion is used as the true LST with the 0 cm surface temperature of the weather station to verify the degree of superiority of the results after the LST downscaling. The root means square error (RMSE) and the coefficient of determination (R^2) are commonly used to test the degree of deviation [51,52]. When the RMSE is smaller and R^2 is larger, it indicates that the RF model LST downscaling results are a more accurate, better fit.

2.4. LCZ and Its Contribution Degree Effect

The LCZ system divides the city limits into building types (LCZ 1–10) and natural cover types (LCZ A–G) according to clear delineation guidelines [53]. With the help of Google Earth's (GE) historical image function, each LCZ category in the Urumqi–Changji–Wujiaqu metropolitan area is judged, and a vector sample is generated. Before participating in the classification, the images are first processed for correction. The classification usually adopts the multiband of L8 OLI; in this study, SI, IBI, NDVI, and MNDWI indexes are added (Tables 1 and 3), which have a significant prominent effect on the urban surface characteristics of arid regions. In addition, principal component analysis is performed on the multispectral bands of OLI and the band information. The first principal component with the largest information load is used for texture analysis. Eight texture information bands based on second-order probability statistics are obtained, which are mean, variance, synergy, contrast, dissimilarity, information entropy, second-order moment, and correlation [54]. Then, based on SAGA GIS software, each of the OLI bands, four index bands, and eight texture information bands are used as data sets to participate in LCZ classification. The final classification raster results are exported to Google Earth for comparison and validation, and 1000 random point validation samples are generated to judge the classification accuracy [55].

Table 3. Remote sensing index calculation.

Variables	Acronym	Formulation
Bare soil index	SI	$\frac{(SWIR+Red)-(NIR+Blue)}{(SWIR+Red)+(NIR+Blue)}$
Index-based built-up index	IBI	$\frac{NDBI-(NDVI+MNDWI)/2}{NDBI+(NDVI+MNDWI)/2}$
Modified normalized difference Water index	MNDWI	$\frac{Green-SWIR}{Green+SWIR}$

The strength of the contribution of different LCZ types to LST varies considerably. The extent to which different LCZ types contribute to urban LST can be quantified using the Contribution Index (CIX) [56]:

$$CIX = (\overline{LST}_n - \overline{LST}_{mean}) \times \left(\frac{S_n}{S} \right) \quad (4)$$

where \overline{LST}_n refers to the average LST of different LCZ landscape types within the study unit n ; \overline{LST}_{mean} is the total average LST of the study unit; S_n is the area of varying LCZ landscape types within that study unit n ; and S is the total area of the study unit. The larger the CIX value (positive numbers are warming contributions and negative numbers are cooling contributions), the higher the degree of its contribution to the surface thermal environment.

2.5. Thermal Environment Network Construction

2.5.1. Identification of Urban Cold Island Patches

The heat accumulation capacity of LST under the large-scale desert substrate in the oasis city in the arid area is remarkable. In contrast, the LST in the oasis area is relatively low, forming a unique microclimate heterogeneous landscape. The contribution of vegetation such as crops, garden trees, flowers, and plants in the oasis area to the constant temperature of LST in the arid area becomes particularly important. Therefore, the results after LST downscaling are divided into five categories using the mean standard deviation method. It is further reclassified into binary pixel data that can be recognized by MSPA, and the cold island region (low and very low temperature) is used as the foreground of MSPA, while the rest is the background. Based on Guidos software, the urban cold island patch landscape types are classified into seven categories, including core, bridge, islet, loop, edge, perforation, and branch (Table 4) [57].

Table 4. MSPA Classification Criteria.

MSPA Class	Meanings
Core	The core is the largest and continuous area of cold island plaques.
Bridge	The role of the bridge is to connect two separate cold island plaques.
Islet	Islets are scattered and independent cold island plaques that are generally small in size.
Loop	Loop functions similarly to bridge but connects different parts of the cold island core.
Edge	Edge is the outer boundary between the cold island and the hot island plaques' contact.
Perforation	Perforation is the inner boundary between the cold island and the hot island plaques' contact.
Branch	The branch is the cold island plaques associated with the edge of the cold island, bridge, and one end of the loop.
Background	Background is the area other than the cold island plaques.

2.5.2. Spatial Network Identification for Thermal Environments

After obtaining the spatial distribution information of cold island patches based on the MSPA method, this paper introduces the circuit theory and Ohm's law to identify the spatial network of the thermal environment in the Urumqi–Changji–Wujiaqu metropolitan area. Circuit theory uses the nature of electrons traveling randomly in a circuit to model the pattern of migration and diffusion of ecological flows or species, etc., in the corridor [39]. In this paper, the LST radiation process is regarded as “current”, and the thermal resistance surface is viewed as a “conductive surface”. In addition, the urban cold island plaques with a core greater than 1 Km² are defined as the source and regarded as a circuit node. LCZ landscapes with a high capacity to store and transmit heat to promote thermal movement (bare ground, dense buildings, etc.) are assigned low resistance, while landscapes with a high capacity to dissipate heat to impede thermal movement (water bodies, high-density vegetation, etc.) are assigned high resistance. The thermal environment of the Urumqi–Changji–Wujiaqu metropolitan area is transformed into a green corridor consisting of “circuit nodes” and “resistance surfaces”. Further, the minimum cost distance to each source is retrieved from the resistive surface using a certain source site as the starting point, and the cumulative current brought about by the circulation of each circuit corridor is calculated [58]. Higher current values indicate high corridor importance levels. The area with high current density values is the thermal environment “pinch point”, indicating that this area is the most effective area for urban cooling and mitigation restoration. One can calculate the accumulated current recovery value of thermal environment obstacle points that hinder the movement of green corridors and identify areas that restrict the connectivity of green networks. This article uses the Linkage Mapper toolbox to identify the green corridor and the Pinchpoint Mapper and Barrier Mapper in the Circuitspace software to identify pinch points and obstacle points in the thermal environment.

2.5.3. Corridor Importance Rating

Surface energy transfer is proportional to source area and current intensity and inversely proportional to corridor length. Therefore, the corridor coefficient is chosen to divide the corridor importance (CI):

$$CI = \frac{Area_{yd} \times \int_s^f Ii}{Length_{Id}} \quad (5)$$

where $Area_{yd}$ is the area of the cold island source site at both ends of the corridor; $\int_s^f Ii$ is the integral of the current intensity from the starting point s to the endpoint f on a corridor; and $Length_{Id}$ is the length of the corridor.

3. Results

3.1. LST Downscaling Features

3.1.1. LST Downscaling Accuracy Verification

Based on the Google Earth engine platform and S2 images, the L8 images with an LST spatial resolution of 30 m were downscaled to 10 m spatial resolution using the RF algorithm. The downscaled LST is combined with L8 LST and weather station LST for accuracy verification. It can be seen that there is a slight gap between the LST inversion results and the LST data of weather stations, which is due to the deviation caused by cloud cover, observation scale, sensor delay error, etc., which is also a certain limitation of LST inversion (Table 5). Furthermore, the RMSE values of LSTsta and LST10m are slightly lower than those of LST30m, indicating that LST at downscaling has the effect of improving the inversion accuracy. It can be seen from Figure 4 that the regression results R^2 of LST30m and LST10m are 0.860, and the fitting degree of the two is also good. This means that the accuracy of the LST downscaling results meets the requirements for subsequent experiments. It is worth noting that even though the surface information of the high-resolution image is used for LST downscaling, some thermal details still have some connection with the original image [59].

Table 5. Comparison of weather station LST with the LST at the same location.

	Station	Station Name	Altitude (m)	Lat N	Lot W	LSTsta	LST30m	LST10m	LSTsta— Δ LST30m	LSTsta— Δ LST10m	
	1	51365	Caijiahu	440.5	44.12	87.32	28.1	29.3	30.1	−1.2	−2
	2	51368	Changji	515.7	44.07	87.19	27.3	28.0	28.6	−0.7	−1.3
	3	51369	Miquan	600.3	43.58	87.39	30.8	33.5	31.9	−2.7	−1.1
	4	51463	Urumqi	935.0	43.47	87.39	28.8	35.4	34.7	−6.6	−5.9
Bias (mean error)									2.8	2.6	
RMSE									3.63	3.23	

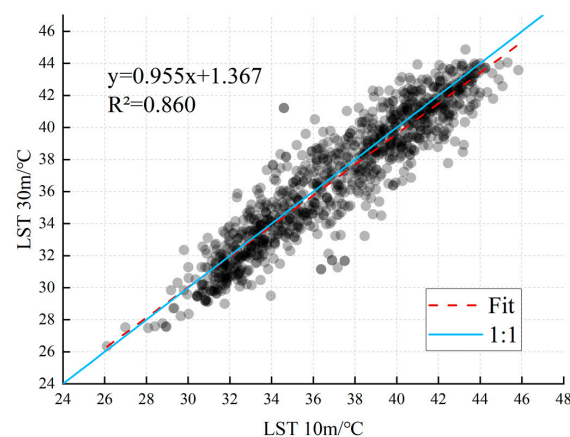


Figure 4. Accuracy verification results of downscaling LST (10 m) and L8 LST (30 m).

To further investigate the relationship between LST before and after downscaling and microscopic urban buildings, the overlay analysis is performed based on the Baidu Map building contours and their floor height data with LST30m and LST10m results, centering on People’s Park and Hongshan Park in Urumqi (Figure 5). And it can be seen that LST10m can achieve a more transparent and detailed expression of urban architecture, which will undoubtedly be of great help to the subsequent analysis of LCZ.

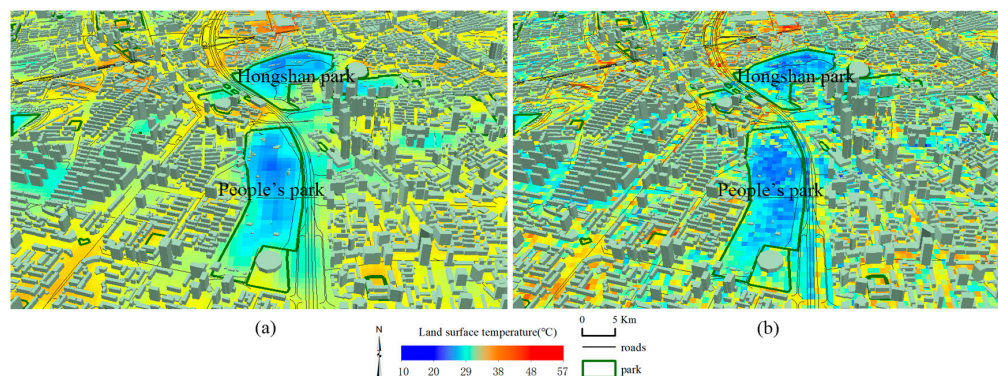


Figure 5. Local 3D architectural map of the study area: (a) is LST30m; (b) is LST10m.

3.1.2. LST10m Spatial Distribution Characteristics

This paper used the mean-standard deviation method to classify the downscaled LST classes (Figure 6). It can be seen from the figure that ELT and LT are primarily distributed in the cultivated land in the north of the study area and MT is distributed mainly in the urban built-up area, while HT and EHT are primarily distributed in the unutilized land in the south of the study area. The study area has a high percentage of HT overall, followed by MT and LT. Among them, HT has the highest proportion of LST in Urumqi City; LT has the highest ratio of LST in Changji City; and MT has the highest LST in Wujiaqu City. This is due to the high level of urbanization in Urumqi City and a certain range of bare land, resulting in a relatively high LST, while Changji City occupies a large area of cultivated land, so the LST is relatively low; Wujiaqu City has no large-scale cultivated land, and the urbanization level is low, so the LST is at the middle level. This means that after neglecting the peripheral landscape (unused land such as desert) of the oasis in the arid zone, the town expansion still causes UHI and is more destructive to the cold and wet climate of the oasis. In addition, from the local map of the city in the study area and combined with the surface parameter information of S2 (Figure 3), it can be seen that the results of LST downscaling inherit the high-resolution urban profile information of S2 better.

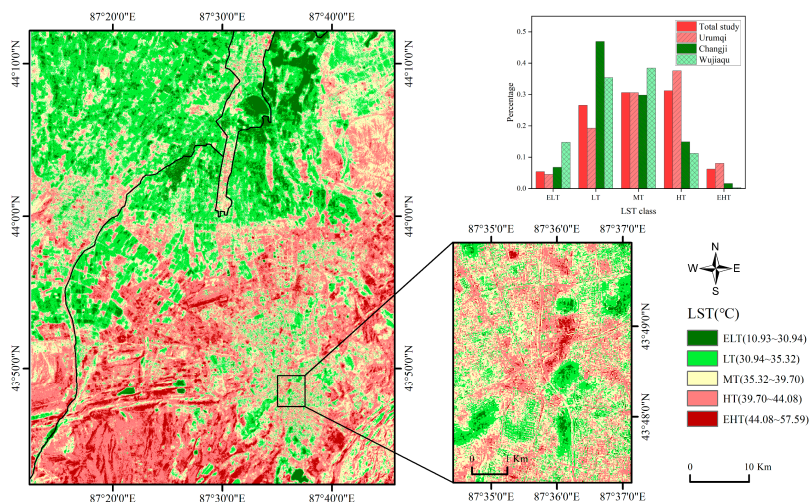


Figure 6. Urumqi–Changji–Wujiaqu metropolitan area LST10m distribution map.

3.2. LCZ Characteristics and Their Contributed Effect on LST

3.2.1. LCZ Classification Accuracy Verification

In this paper, about 2000 vector training samples are selected in the same period of GE to obtain the preliminary classification results of LCZ, and the classification results are led back to GE for class-by-class superposition. The sample points with errors in classification are resampled to finally obtain the LCZ classification map (Figure 7). Then, using the high-resolution images of GE, we select randomly sampled 1000 sample points for accuracy verification, and the total classification accuracy (OA) is obtained as 83.1% with a Kappa coefficient of 0.804 (Table 6). The results of user accuracy and producer accuracy show that the natural classification accuracy (A–G) of LCZ is higher than the building classification accuracy (1–10). This is due to the large area and single type of natural feature type, while the classification standards of building types are detailed and the distribution is compact, so the error caused by building types is high. The phenomenon of “different things with the same spectrum” in the spectral curves of the features also has some influence on the misclassification of LCZ. Overall, the LCZ classification meets the accuracy requirements.

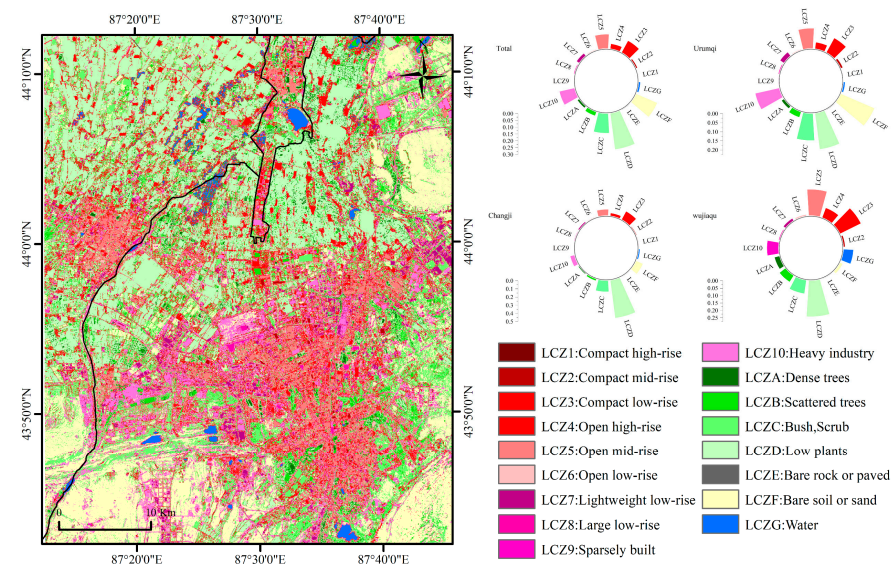


Figure 7. Local climate zone map.

Table 6. Local climate zoning accuracy evaluation table.

LCZ Class	1	2	3	4	5	6	7	8	9	10	A	B	C	D	E	F	G	Row Pixels	User Acc (%)
1	4	1	0	0	0	0	0	0	0	0	0	0	0	0	0	0	0	5	80
2	0	9	0	1	1	0	1	0	0	1	0	0	1	0	1	0	0	15	60
3	0	0	36	1	4	0	2	0	2	4	0	4	20	4	4	3	0	84	43
4	0	0	0	14	4	0	1	0	0	1	0	3	4	0	3	0	0	30	47
5	0	2	2	0	74	0	1	0	1	2	1	3	6	6	4	3	0	105	70
6	0	0	0	0	1	4	0	0	0	0	0	0	1	0	0	0	0	6	67
7	0	0	0	0	1	0	23	0	0	0	0	0	1	0	0	0	0	25	92
8	0	0	0	0	0	0	0	6	0	0	0	0	2	0	0	0	0	8	75
9	0	0	0	0	0	0	0	0	2	0	0	0	0	0	0	0	0	2	00
10	0	1	0	2	5	0	0	0	0	75	0	1	11	1	3	3	1	103	73
A	0	0	0	0	0	0	0	0	0	0	13	0	0	3	0	0	0	16	81
B	0	0	0	0	0	0	0	0	0	0	0	40	0	1	0	0	0	41	98
C	0	0	0	1	2	0	0	0	0	1	0	1	140	0	1	0	0	146	96
D	0	0	0	1	4	0	0	0	0	0	5	10	0	225	0	0	0	245	92
E	0	0	0	0	0	0	0	0	0	0	0	0	0	0	3	0	0	3	00
F	0	0	1	0	0	0	0	0	1	0	0	0	0	1	0	155	0	158	98
G	0	0	0	0	0	0	0	0	0	0	0	0	0	0	0	0	8	8	00
Column pixels	4	13	39	20	96	4	28	6	6	84	19	62	186	241	19	164	9	1000	Kappa:0.804
Producer acc (%)	00	62	92	70	77	00	82	00	33	89	68	65	75	93	16	95	89		

3.2.2. Characteristics of LCZ Spatial Distribution and Its Relationship with LST

As seen in Figure 7, the study area has the largest proportion of natural types LCZ-D, LCZ-F, and LCZ-C, while it has the largest proportion of building types LCZ-5, LCZ-10, and LCZ-3. The metropolitan area has fewer high-rise buildings and mostly mid-rise and low-rise buildings, with a medium to high level of urban development and a weaker overall development force than the coastal cities in eastern China. The urban buildings in Urumqi are distributed in a “T” shape, and the factories and lightweight buildings (containers, etc.) in the metropolitan area are mainly spread around the central city of Urumqi, with a high level of industrial development. Changji and Wujiaqu cities are less urbanized; LCZ-D is the primary land use type, while LCZ-3 is presented in a rural form, mainly concentrated between cities and towns.

Overlaying the LCZ results with the LST10m, we can see that the mean LST values are higher for building types LCZ-2, LCZ-7, LCZ-8, LCZ-9, and LCZ-10 and natural types LCZ-C, LCZ-E, and LCZ-F (Figure 8). The building type is mainly warming caused by impervious surfaces such as asphalt, while the high temperature of the natural type is mostly heat gathering caused by bare sand and hay-like vegetation. Comparing the temperature statistics, it is found that the LST in the Urumqi–Changji–Wujiaqu metropolitan area shows a changing pattern of high-rise < low-rise < mid-rise for both “dense” and “open” building types (LCZ1–LCZ6). In addition, LCZ7–LCZ10 building types have a higher impact on LST. The difference in the effects of urban building type on LST is evident.

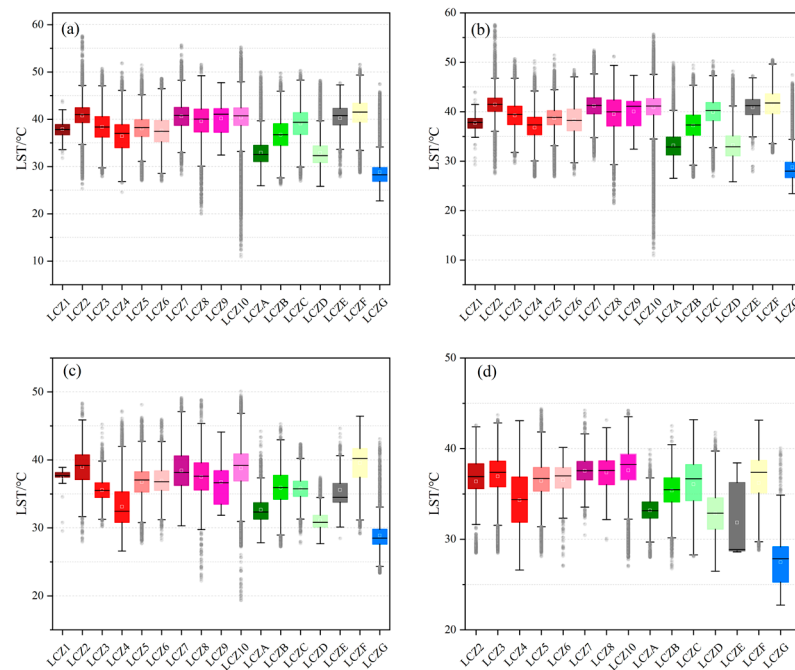


Figure 8. LCZ and LST box line diagram: (a) the total study area; (b) Urumqi city; (c) Changji city; (d) Wujiaqu city.

3.2.3. Contribution Effect of LCZ on LST

The contribution index is introduced in this paper to explore the contribution of LCZ type on LST warming/cooling (Figure 9). We can see from the results that LCZ-D contributes the most to the cooling effect of LST, followed by LCZ-G, LCZ-4, and LCZ-A. LCZ-F contributed the most to the heating effect of LST, followed by LCZ-C, LCZ-1, LCZ-3, LCZ-5, and LCZ-7. The contribution of the LCZ to the LST is not only the nature of the underlying surface of the ground object itself, but it also has a great relationship with the area of the study area occupied by the LCZ.

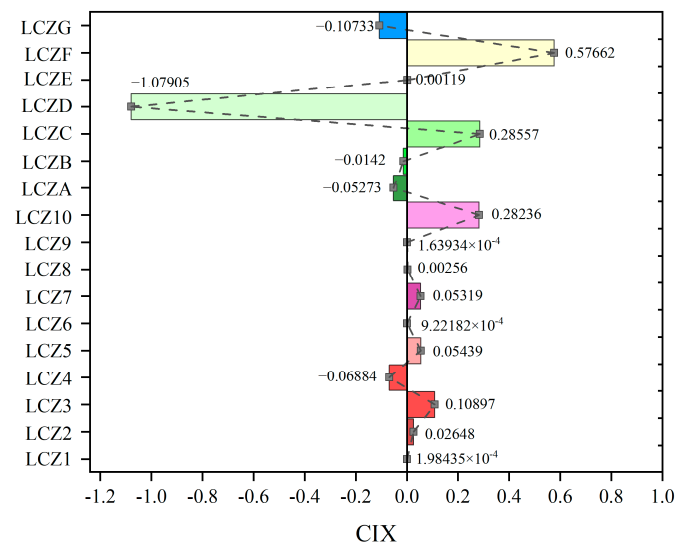


Figure 9. Comparison of LCZ increase/decrease temperature contribution.

3.3. Analysis of Urban Thermal Environment Networks and Key Corridors

3.3.1. MSPA-Based Cold Island Plaques Identification

We identify cold island patches in the Urumqi–Changji–Wujiaqu metropolitan area based on MSPA and classify them into seven types (Figure 10a). Overall, the core type is the primary type of cold island patch, with an area of about 630.38 km², accounting for 57.49% of the area of cold island patches and 18.39% of the total area of the whole study area (Table 7). In the theory of spatial morphology, the size of the core type determines the stability of the network, and the core of the cold island is generally covered with arable land, forest land, and water bodies. The second is the perforation type, which is located in the area where the hot and cold islands meet, accounting for 15.02% and 4.81% of the cold island patch and the overall study area, respectively. The following categories are bridge, loop, edge, and branch, which account for 8.96%, 6.95%, 5.37%, and 4.04% of the cold island patches, respectively. Islets accounted for the lowest proportion of the MSPA category, accounting for only 2.17% of the total cold island patches and 0.69% of the study area.

Table 7. MSPA Statistics Table.

MSPA Class	Area (km ²)	Total Area of the Cold Island Patches (%)	Total Study Area (%)
Core	630.38	57.49	18.39
Bridge	98.20	8.96	2.86
Islet	23.76	2.17	0.69
Loop	76.24	6.95	2.22
Edge	58.88	5.37	1.72
Perforation	164.72	15.02	4.81
Branch	44.31	4.041	1.29

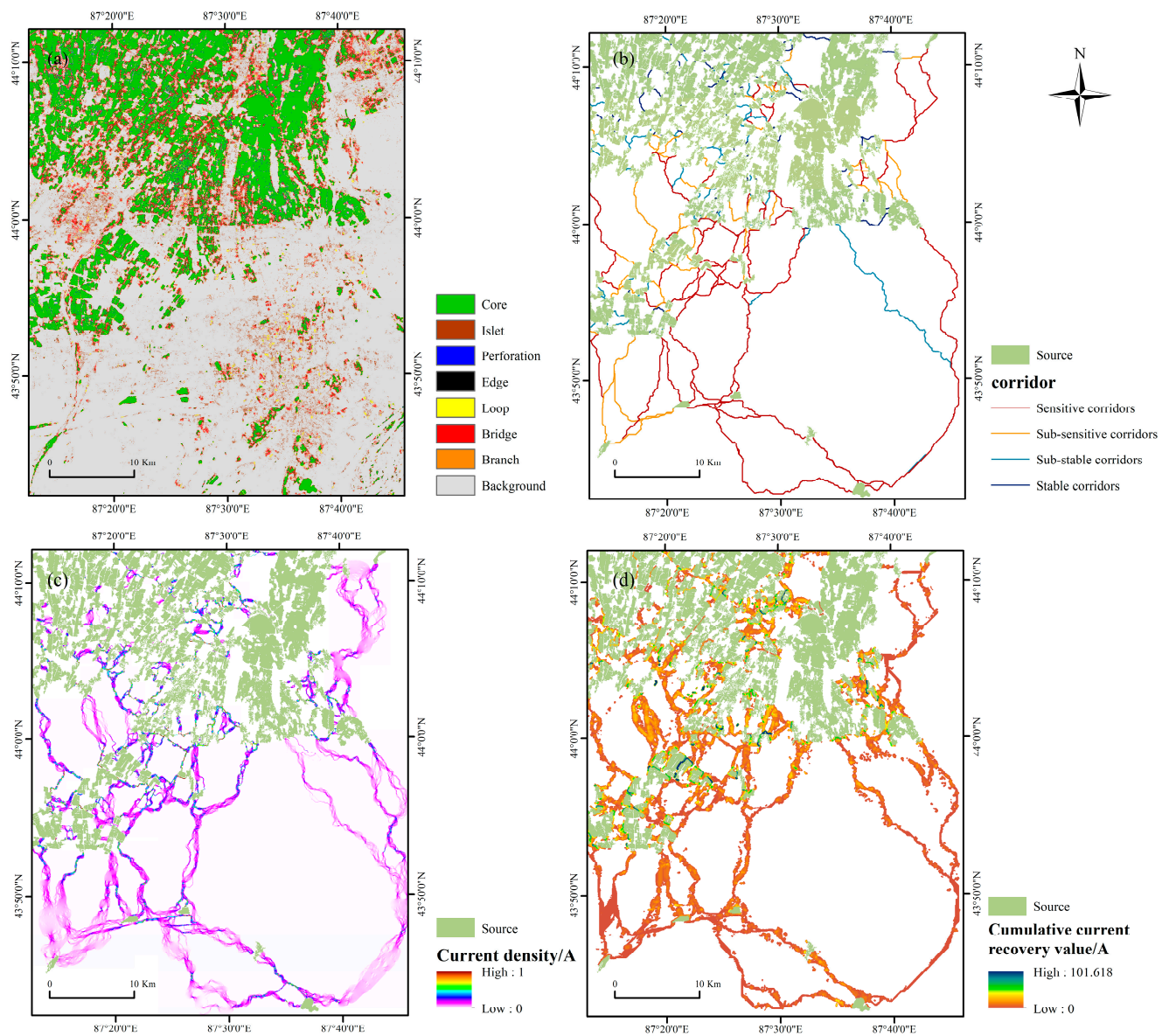


Figure 10. Green corridor, pinch point, and obstacle point identification for the thermal environment based on MSPA and circuit theory: (a) cold island patch classification based on MSPA; (b) green corridor identification and importance classification; (c) key pinch point identification; (d) key obstacle point identification.

3.3.2. Thermal Environment Green Corridor and Its Grade Analysis

Before determining the corridor, in this paper, based on the contribution index, it is judged whether each LCZ type is conducive to land surface energy transmission and according to the ratio to give different resistance values. That is, LCZ-D has the highest cooling contribution to LST, indicating that it is easy to diffuse land surface thermal energy, and it is assigned the highest resistance coefficient; LCZ-F has the most increased warming contribution to LST, suggesting that it is easy to store land surface thermal energy, and it is assigned the lowest resistance coefficient (Table 8).

Table 8. LCZ-based resistance values for cold island plaques.

LCZ Class	Resistance Value	LCZ Class	Resistance Value
LCZ1	15	LCZ10	5
LCZ2	10	LCZA	30
LCZ3	10	LCZB	25
LCZ4	30	LCZC	5
LCZ5	10	LCZD	100
LCZ6	15	LCZE	15
LCZ7	10	LCZF	1
LCZ8	15	LCZG	50
LCZ9	15		

According to the corridor coefficient and equal spacing method, the thermal environment green corridors are classified into four categories (Figure 10b). The path from one source to another is affected by inhomogeneous extension resistance, so the shortest path between sources is not a straight line but the result of a combined calculation of resistance surfaces. The total number of green corridors in the study area is 253, and the greater the distance between two cold island patches, the higher the degree of sensitivity of the corridors. The substable corridors and stable corridors are mainly distributed in the cold island patches in the northern part of the study area. Sensitive green corridors are vulnerable to destruction by human activities, and the identification of green corridor paths can effectively protect and maintain them.

3.3.3. Green Corridor Analysis and Restoration

Based on the results of green corridor extraction, the “all-to-one” mode in the pinch point mapper is invoked to identify the pinch point area (Figure 10c); the minimum search radius of 30 m and the maximum search radius of 120 m is used to determine the obstacle points (Figure 10d). The value range of the green corridor’s current intensity is [0~1] A. The average value of the current intensity is about 0.01 A. The pinch point is a region with a high current density concentration, primarily distributed in rural areas within the study area. The mean value of regional cumulative current recovery is 5.34 A, and the high-value area is mainly distributed between cultivated land and cultivated land (mostly areas where villages are gathered), which is a hindrance to corridor connectivity and surface heat dissipation.

4. Discussion

4.1. Relationship between LCZ and LST in Arid Zones and Their Cooling Measures

Compared with the traditional land use classification (six significant categories such as cropland, forest land, grassland, construction land, water bodies, and unused land), LCZ has extremely fine delineation for surface cover [60,61]. In particular, the building types cover almost all urban space buildings. Therefore, the study combining LST downscaling with LCZ can effectively shrink the errors caused by spatial scale mismatch. In this study, the positive and negative contribution effects of 17 categories of LCZ on LST are basically consistent with previous studies [33]. However, a particular category of natural types deserves our attention, that is LCZ-C (mainly grassland with low coverage), which has a positive effect on LST and occupies a large proportion, which is inconsistent with previous studies. The occurrence of this phenomenon is strongly associated with the climatic characteristics of the arid zone. The average annual precipitation in arid areas is less than 200 mm, and with the high temperature for water vapor consumption, evapotranspiration is high, so vegetation is generally sparse and usually dominated by drought-resistant short-growth plants (haloxylon ammodendron, alhagi sparsifolia shap, tamarix chinensis lour, etc.) [62]. Although LCZ-C belongs to vegetation, its cooling ability to LST is limited. In contrast, the cooling contribution of LCZ-D to LST is the most significant, coupled with

the fact that the study area is a typical agricultural oasis, so agricultural irrigation and arable land conservation are the primary means of maintaining the oasis's cold island.

Different building types have different contribution effects on LST. Dense urban space buildings have poorer ventilation effects and higher temperature concentrations than open buildings [29]. Therefore, on the premise of ensuring the allocation and supply of land resources that are in short supply within the city, natural elements such as vegetation and water bodies can be assigned to dense building areas as a priority in urban space planning. In addition, in the process of selecting the area of interest, we found that a large part of the dense middle-rise buildings are old residential areas or urban villages. The high building density and population density in these areas are not conducive to human thermal comfort [63]. Effective urban renewal is required, such as widening roads or transforming them into mid-rise and open buildings. It is important to emphasize that a higher number of floors in a building is not better. Although high-rise buildings are suitable for urban ventilation, they have certain safety risks when elevators fail or in case of fire. Therefore, promoting the construction of local blue-green space is the key to improving the urban thermal environment.

4.2. Protection and Optimization of Green Space in the Metropolitan Area

As the political and economic center of "One Belt and One Road" construction in Xinjiang and even Northwest China, the influence and radiation of the Urumqi–Changji–Wujiaqu metropolitan area is undoubtedly massive [64]. This paper chooses a combination of MSPA and circuit theory to be applied to urban heat island research. The construction of green corridors for the urban thermal environment from the perspective of combining urban and rural gradients can enhance the connectivity of cold source landscapes and maintain the security of the regional thermal environment [39]. In the present study, we identify 253 green corridors, and planners and decision-makers need to take certain precautions when implementing plans for urban construction, focusing on the degree of sensitivity of the corridors, as blockage of the corridors will further exacerbate the UHI intensity [40]. In addition, the ecological background characteristics of the pinch point area are good, and it is recommended that natural protection be the main focus, supplemented by human restoration, including measures such as developing unused land into arable land or stopping construction land from encroaching on cropland. Furthermore, human activities are frequent in the ecological obstacle area. In order to reduce the ecological flow resistance and effectively improve the landscape connectivity, it is recommended to adopt a method of equal emphasis on artificial restoration and natural protection, including building reservoirs or planting high-coverage forests and shrubs in the obstacle area.

4.3. Limitations and Prospects for the Future

First, the Urumqi–Changji–Wujiaqu metropolitan area is at the intersection of multiple image coverage. Since the accuracy of LST downscaling of the L8 image will be significantly reduced after image stitching, and the research scope has covered the main urban buildings, this paper only selects a single image of L8 for analysis. In future work, we will continue to optimize the LST downscaling algorithm to achieve large-scale downscaling of LST. Second, limited by the launch time of S2 satellite L2A, this paper only performs downscaling analysis of the summer 2021 LST, which can be combined with subsequent images of S2 in future work or can resample L8 to high spatial resolution as an auxiliary surface parameter to improve the temporal resolution of the study. And last, the construction of the resistance surface in this paper contains information on the two-dimensional and three-dimensional level of the city, and the influence of the topography and elevation, etc., are ignored. Although the topography of the Urumqi–Changji–Wujiaqu metropolitan area is flat, and the terrain is not highly undulating, there are still some errors. In future work, the factors that affect LST can be ranked and incorporated into constructing the thermal environment resistance surface.

5. Conclusions

The background of rapid urbanization has a more substantial impact on arid areas, and how to moderately cool local places is the focus of the academic community. This study proposes to combine L8 and S2 for LST downscaling and then construct a thermal environment resistance surface based on LCZ to form a regionally integrated cooling network, which is rarely performed in previous studies. The results showed that ELT and LT were mainly distributed in arable land (LCZ-D), high cover degree vegetation (LCZ-A, LCZ-B), and water bodies (LCZ-G), HT was distributed primarily on residential areas of built-up land (LCZ1-LCZ6), HT and very high temperature were mainly distributed in factories of built-up land (LCZ7-LCZ10), low cover degree grassland (LCZ-C) and bare (LCZ-C) and bare land (LCZ-F). A total of 253 green corridors in the thermal environment network were identified using circuit theory. The longer the distance between cold sources, the higher the degree of sensitivity of the corridors. Combined with the locations of pinch points and obstacle points in the thermal environment network, policymakers applied the corresponding measures of protection and repair to relieve the thermal pressure in the metropolitan area. In addition to providing a scientific basis for urban planners in arid zones to mitigate extreme urban heat waves in terms of building type and regional integration, the study can also be applied to every city at thermal risk. With the process of global integration, the continued elevation of LST will face even greater challenges.

Author Contributions: Conceptualization and methodology, X.Z. and A.K.; software, H.L.; resources, B.W. and Y.A.; supervision, Y.Z. and R.R. All authors have read and agreed to the published version of the manuscript.

Funding: This research was funded by the Third Xinjiang Scientific Expedition Program, grant number NO. 2021xjkk0905, and the Special Project for the Construction of Innovation Environment in the Autonomous Region, grant number NO. 2022D04007.

Data Availability Statement: Data are contained within the article.

Acknowledgments: The authors are grateful to the reviewers for their constructive comments.

Conflicts of Interest: The authors declare no conflict of interest. The funders had no role in the design of the study; in the collection, analyses, or interpretation of data; in the writing of the manuscript; or in the decision to publish the results.

References

1. Pal, S.; Ziaul, S.K. Detection of land use and land cover change and land surface temperature in English Bazar urban centre. *Egypt. J. Remote Sens. Space Sci.* **2017**, *20*, 125–145. [[CrossRef](#)]
2. Zhang, X.; Kasimu, A.; Liang, H.; Wei, B.; Aizzizi, Y. Spatial and Temporal Variation of Land Surface Temperature and Its Spatially Heterogeneous Response in the Urban Agglomeration on the Northern Slopes of the Tianshan Mountains, Northwest China. *Int. J. Environ. Res. Public Health* **2022**, *19*, 13067. [[CrossRef](#)] [[PubMed](#)]
3. Nuruzzaman, M. Urban Heat Island: Causes, Effects and Mitigation Measures—A Review. *Int. J. Environ. Monit. Anal.* **2015**, *3*, 67–73.
4. Oke, T.R. City size and the urban heat island. *Atmos. Environ.* **1973**, *7*, 769–779. [[CrossRef](#)]
5. He, B.-J.; Wang, J.; Liu, H.; Ulpiani, G. Localized synergies between heat waves and urban heat islands: Implications on human thermal comfort and urban heat management. *Environ. Res.* **2021**, *193*, 110584. [[CrossRef](#)]
6. Arnfield, A.J. Two decades of urban climate research: A review of turbulence, exchanges of energy and water, and the urban heat island. *Int. J. Climatol.* **2003**, *23*, 1–26. [[CrossRef](#)]
7. Estoque, R.C.; Murayama, Y.; Myint, S.W. Effects of landscape composition and pattern on land surface temperature: An urban heat island study in the megacities of Southeast Asia. *Sci. Total Environ.* **2017**, *577*, 349–359. [[CrossRef](#)]
8. Manoli, G.; Fatichi, S.; Schlapfer, M.; Yu, K.L.; Crowther, T.W.; Meili, N.; Burlando, P.; Katul, G.G.; Bou-Zeid, E. Magnitude of urban heat islands largely explained by climate and population. *Nature* **2019**, *573*, 55–60. [[CrossRef](#)]
9. U.S. Environmental Protection Agency. Reducing Urban Heat Islands: Compendium of Strategies. Draft; 2008. Available online: <https://www.epa.gov/heat-islands/heat-island-compendium> (accessed on 10 November 2022).
10. Ulpiani, G. On the linkage between urban heat island and urban pollution island: Three-decade literature review towards a conceptual framework. *Sci. Total Environ.* **2021**, *751*, 141727. [[CrossRef](#)]
11. Nwakaire, C.M.; Onn, C.C.; Yap, S.P.; Yuen, C.W.; Onodagu, P.D. Urban Heat Island Studies with emphasis on urban pavements: A review. *Sust. Cities Soc.* **2020**, *63*, 102476. [[CrossRef](#)]

12. Sobrino, J.A.; Jiménez-Muñoz, J.C.; Paolini, L. Land surface temperature retrieval from LANDSAT TM 5. *Remote Sens. Environ.* **2004**, *90*, 434–440. [[CrossRef](#)]
13. Vlassova, L.; Perez-Cabello, F.; Nieto, H.; Martín, P.; Riaño, D.; De La Riva, J. Assessment of methods for land surface temperature retrieval from Landsat-5 TM images applicable to multiscale tree-grass ecosystem modeling. *Remote Sens.* **2014**, *6*, 4345–4368. [[CrossRef](#)]
14. Weng, Q.; Fu, P.; Gao, F. Generating daily land surface temperature at Landsat resolution by fusing Landsat and MODIS data. *Remote Sens. Environ.* **2014**, *145*, 55–67. [[CrossRef](#)]
15. Jamali, A.A.; Kalkhajeh, R.G.; Randhir, T.O.; He, S. Modeling relationship between land surface temperature anomaly and environmental factors using GEE and Giovanni. *J. Environ. Manag.* **2022**, *302*, 113970. [[CrossRef](#)] [[PubMed](#)]
16. Bechtel, B.; Zakšek, K.; Hoshyaripour, G. Downscaling land surface temperature in an urban area: A case study for Hamburg, Germany. *Remote Sens.* **2012**, *4*, 3184–3200. [[CrossRef](#)]
17. Zakšek, K.; Oštir, K. Downscaling land surface temperature for urban heat island diurnal cycle analysis. *Remote Sens. Environ.* **2012**, *117*, 114–124. [[CrossRef](#)]
18. Pu, R.; Bonafoni, S. Reducing Scaling Effect on Downscaled Land Surface Temperature Maps in Heterogenous Urban Environments. *Remote Sens.* **2021**, *13*, 5044. [[CrossRef](#)]
19. Wang, S.; Luo, Y.; Li, M.; Yang, K.; Liu, Q.; Li, X. A Taylor expansion algorithm for spatial downscaling of MODIS land surface temperature. *IEEE Trans. Geosci. Remote Sens.* **2022**, *60*, 5002717. [[CrossRef](#)]
20. Zawadzka, J.; Corstanje, R.; Harris, J.; Truckell, I. Downscaling Landsat-8 land surface temperature maps in diverse urban landscapes using multivariate adaptive regression splines and very high resolution auxiliary data. *Int. J. Digit. Earth* **2020**, *13*, 899–914. [[CrossRef](#)]
21. Kustas, W.P.; Norman, J.M.; Anderson, M.C.; French, A.N. Estimating subpixel surface temperatures and energy fluxes from the vegetation index–radiometric temperature relationship. *Remote Sens. Environ.* **2003**, *85*, 429–440. [[CrossRef](#)]
22. Essa, W.; van der Kwast, J.; Verbeiren, B.; Batelaan, O. Downscaling of thermal images over urban areas using the land surface temperature–impervious percentage relationship. *Int. J. Appl. Earth Observat. Geoinform.* **2013**, *23*, 95–108. [[CrossRef](#)]
23. Agam, N.; Kustas, W.P.; Anderson, M.C.; Li, F.; Neale, C.M.U. A vegetation index based technique for spatial sharpening of thermal imagery. *Remote Sens. Environ.* **2007**, *107*, 545–558. [[CrossRef](#)]
24. Dominguez, A.; Kleissl, J.; Luvall, J.C.; Rickman, D.L. High-resolution urban thermal sharpener (HUTS). *Remote Sens. Environ.* **2011**, *115*, 1772–1780. [[CrossRef](#)]
25. Ebrahimi, H.; Azadbakht, M. Downscaling MODIS land surface temperature over a heterogeneous area: An investigation of machine learning techniques, feature selection, and impacts of mixed pixels. *Comput. Geosci.* **2019**, *124*, 93–102. [[CrossRef](#)]
26. Hutengs, C.; Vohland, M. Downscaling land surface temperatures at regional scales with random forest regression. *Remote Sens. Environ.* **2016**, *178*, 127–141. [[CrossRef](#)]
27. Li, W.; Ni, L.; Li, Z.-L.; Duan, S.-B.; Wu, H. Evaluation of machine learning algorithms in spatial downscaling of MODIS land surface temperature. *IEEE J. Sel. Topic. Appl. Earth Observat. Remote Sens.* **2019**, *12*, 2299–2307. [[CrossRef](#)]
28. Richard, Y.; Emery, J.; Dudek, J.; Pergaud, J.; Chateau-Smith, C.; Zito, S.; Rega, M.; Vairet, T.; Castel, T.; Thévenin, T. How relevant are local climate zones and urban climate zones for urban climate research? Dijon (France) as a case study. *Urban Clim.* **2018**, *26*, 258–274. [[CrossRef](#)]
29. Mushore, T.D.; Mutanga, O.; Odindi, J. Determining the Influence of Long Term Urban Growth on Surface Urban Heat Islands Using Local Climate Zones and Intensity Analysis Techniques. *Remote Sens.* **2022**, *14*, 2060. [[CrossRef](#)]
30. Zhuang, Q.; Wu, S.; Yan, Y.; Niu, Y.; Yang, F.; Xie, C. Monitoring land surface thermal environments under the background of landscape patterns in arid regions: A case study in Aksu river basin. *Sci. Total Environ.* **2020**, *710*, 136336. [[CrossRef](#)]
31. Perera, N.G.R.; Emmanuel, R. A “Local Climate Zone” based approach to urban planning in Colombo, Sri Lanka. *Urban Clim.* **2018**, *23*, 188–203. [[CrossRef](#)]
32. Stewart, I.D.; Oke, T.R. Local climate zones for urban temperature studies. *Bull. Am. Meteorol. Soc.* **2012**, *93*, 1879–1900. [[CrossRef](#)]
33. Demuzere, M.; Hankey, S.; Mills, G.; Zhang, W.; Lu, T.; Bechtel, B. Combining expert and crowd-sourced training data to map urban form and functions for the continental US. *Sci. Data* **2020**, *7*, 264. [[CrossRef](#)] [[PubMed](#)]
34. Ching, J.; Mills, G.; Bechtel, B.; See, L.; Feddema, J.; Wang, X.; Ren, C.; Brousse, O.; Martilli, A.; Neophytou, M. WUDAPT: An urban weather, climate, and environmental modeling infrastructure for the anthropocene. *Bull. Am. Meteorol. Soc.* **2018**, *99*, 1907–1924. [[CrossRef](#)]
35. Luo, G.; Lu, L.; Yin, C.; Feng, Y. An analysis of oasis stability in arid areas: A case study in the northern slope areas of the Tianshan Mountains. *J. Arid Land* **2009**, *1*, 49–56.
36. Feyisa, G.L.; Dons, K.; Meilby, H. Efficiency of parks in mitigating urban heat island effect: An example from Addis Ababa. *Landsc. Urban Plan.* **2014**, *123*, 87–95. [[CrossRef](#)]
37. Liu, W.; Zhao, H.Y.; Sun, S.B.; Xu, X.Y.; Huang, T.T.; Zhu, J.N. Green space cooling effect an contribution to mitigate heat island of surrounding communities in Beijing Metropolitan Area. *Front. Public Health* **2022**, *10*, 870403. [[CrossRef](#)]
38. Estoque, R.C.; Ooba, M.; Seposo, X.T.; Togawa, T.; Hijjoka, Y.; Takahashi, K.; Nakamura, S. Heat health risk assessment in Philippine cities using remotely sensed data and social-ecological indicators. *Nat. Commun.* **2020**, *11*, 1581. [[CrossRef](#)]
39. Yu, Z.; Zhang, J.; Yang, G. How to build a heat network to alleviate surface heat island effect? *Sust. Cities Soc.* **2021**, *74*, 103135. [[CrossRef](#)]

40. Peng, J.; Cheng, X.; Hu, Y.; Corcoran, J. A landscape connectivity approach to mitigating the urban heat island effect. *Landscape Ecol.* **2022**, *37*, 1707–1719. [[CrossRef](#)]
41. Loménié, N.; Racoceanu, D. Point set morphological filtering and semantic spatial configuration modeling: Application to microscopic image and bio-structure analysis. *Pattern Recognit.* **2012**, *45*, 2894–2911. [[CrossRef](#)]
42. Rogan, J.; Wright, T.M.; Cardille, J.; Pearsall, H.; Ogneva-Himmelberger, Y.; Riemann, R.; Riitters, K.; Partington, K. Forest fragmentation in Massachusetts, USA: A town-level assessment using Morphological spatial pattern analysis and affinity propagation. *GISci. Remote Sens.* **2016**, *53*, 506–519. [[CrossRef](#)]
43. Kang, J.; Li, C.; Li, M.; Zhang, T.; Zhang, B. Identifying priority areas for conservation in the lower Yellow River basin from an ecological network perspective. *Ecosyst. Health Sust.* **2022**, *8*, 2105751. [[CrossRef](#)]
44. Zhao, Y.; Kasimu, A.; Liang, H.; Reheman, R. Construction and restoration of landscape ecological network in urumqi city based on landscape ecological risk assessment. *Sustainability* **2022**, *14*, 8154. [[CrossRef](#)]
45. Kotték, M.; Grieser, J.; Beck, C.; Rudolf, B.; Rubel, F. World map of the Köppen-Geiger climate classification updated. *Meteorol. Z.* **2006**, *15*, 259–263. [[CrossRef](#)]
46. Breiman, L. Random forests. *Mach. Learn.* **2001**, *45*, 5–32. [[CrossRef](#)]
47. Noi, P.T.; Degener, J.; Kappas, M. Comparison of multiple linear regression, cubist regression, and random forest algorithms to estimate daily air surface temperature from dynamic combinations of MODIS LST data. *Remote Sens.* **2017**, *9*, 398. [[CrossRef](#)]
48. Sussman, H.S.; Dai, A.; Roundy, P.E. The controlling factors of urban heat in Bengaluru, India. *Urban Clim.* **2021**, *38*, 100881. [[CrossRef](#)]
49. Im, J.; Park, S.; Rhee, J.; Baik, J.; Choi, M. Downscaling of AMSR-E soil moisture with MODIS products using machine learning approaches. *Environ. Earth Sci.* **2016**, *75*, 1–19. [[CrossRef](#)]
50. Sekertekin, A. Validation of physical radiative transfer equation-based land surface temperature using Landsat 8 satellite imagery and SURFRAD in-situ measurements. *J. Atmos. Sol. Terr. Phys.* **2019**, *196*, 105161. [[CrossRef](#)]
51. Draper, C.; Reichle, R.; de Jeu, R.; Naeimi, V.; Parinussa, R.; Wagner, W. Estimating root mean square errors in remotely sensed soil moisture over continental scale domains. *Remote Sens. Environ.* **2013**, *137*, 288–298. [[CrossRef](#)]
52. Nakagawa, S.; Schielzeth, H. A general and simple method for obtaining R² from generalized linear mixed-effects models. *Methods Ecol. Evol.* **2013**, *4*, 133–142. [[CrossRef](#)]
53. Yang, J.; Jin, S.; Xiao, X.; Jin, C.; Xia, J.C.; Li, X.; Wang, S. Local climate zone ventilation and urban land surface temperatures: Towards a performance-based and wind-sensitive planning proposal in megacities. *Sust. Cities Soc.* **2019**, *47*, 101487. [[CrossRef](#)]
54. Xu, Y.; Ren, C.; Cai, M.; Edward, N.Y.Y.; Wu, T. Classification of local climate zones using ASTER and Landsat data for high-density cities. *IEEE J. Sel. Topic. Appl. Earth Observat. Remote Sens.* **2017**, *10*, 3397–3405. [[CrossRef](#)]
55. Wang, R.; Wang, M.; Zhang, Z.; Hu, T.; Xing, J.; He, Z.; Liu, X. Geographical Detection of Urban Thermal Environment Based on the Local Climate Zones: A Case Study in Wuhan, China. *Remote Sens.* **2022**, *14*, 1067. [[CrossRef](#)]
56. Ayanlade, A.; Aigbiremolen, M.I.; Oladosu, O.R. Variations in urban land surface temperature intensity over four cities in different ecological zones. *Sci. Rep.* **2021**, *11*, 20537. [[CrossRef](#)]
57. Carlier, J.; Moran, J. Landscape typology and ecological connectivity assessment to inform Greenway design. *Sci. Total Environ.* **2019**, *651*, 3241–3252. [[CrossRef](#)]
58. Leonard, P.B.; Duffy, E.B.; Baldwin, R.F.; McRae, B.H.; Shah, V.B.; Mohapatra, T.K. gflow: Software for modelling circuit theory-based connectivity at any scale. *Method. Ecol. Evol.* **2017**, *8*, 519–526. [[CrossRef](#)]
59. Bonafoni, S.; Anniballe, R.; Gioli, B.; Toscano, P. Downscaling Landsat land surface temperature over the urban area of Florence. *Eur. J. Remote Sens.* **2016**, *49*, 553–569. [[CrossRef](#)]
60. Zheng, Y.; Ren, C.; Xu, Y.; Wang, R.; Ho, J.; Lau, K.; Ng, E. GIS-based mapping of Local Climate Zone in the high-density city of Hong Kong. *Urban Clim.* **2018**, *24*, 419–448. [[CrossRef](#)]
61. Aizizi, Y.; Kasimu, A.; Liang, H.W.; Zhang, X.L.; Zhao, Y.Y.; Wei, B.H. Evaluation of ecological space and ecological quality changes in urban agglomeration on the northern slope of the Tianshan Mountains. *Ecol. Indic.* **2023**, *146*, 109896. [[CrossRef](#)]
62. Yao, J.; Yang, Q.; Mao, W.; Zhao, Y.; Xu, X. Precipitation trend–Elevation relationship in arid regions of the China. *Glob. Planet. Chang.* **2016**, *143*, 1–9. [[CrossRef](#)]
63. Jin, L.; Pan, X.; Liu, L.; Liu, L.; Liu, J.; Gao, Y. Block-based local climate zone approach to urban climate maps using the UDC model. *Build. Environ.* **2020**, *186*, 107334. [[CrossRef](#)]
64. Liang, H.; Kasimu, A.; Ma, H.; Zhao, Y.; Zhang, X.; Wei, B. Exploring the Variations and Influencing Factors of Land Surface Temperature in the Urban Agglomeration on the Northern Slope of the Tianshan Mountains. *Sustainability* **2022**, *14*, 10663. [[CrossRef](#)]

Disclaimer/Publisher’s Note: The statements, opinions and data contained in all publications are solely those of the individual author(s) and contributor(s) and not of MDPI and/or the editor(s). MDPI and/or the editor(s) disclaim responsibility for any injury to people or property resulting from any ideas, methods, instructions or products referred to in the content.